Design And Dynamic Analysis of a Delta Robot

Mohammad Basheeruddin[1], K. T. Balaram Padal[2]

[1]*Post Graduation Student, Department of Mechanical Engineering [Machine Design], AU College of Engineering (A), Andhra University, Visakhapatnam – 530003, Andhra Pradesh, India*

[2]*Professor, Department of Mechanical Engineering, AU College of Engineering (A), Andhra University, Visakhapatnam – 530003, Andhra Pradesh, India*

***Abstract*—Delta robots are parallel manipulators in which three kinematic chains carry a light moving platform from base-mounted actuators, which makes them well suited to fast pick-and-place work. A three-degree-of-freedom translational Delta robot based on a published configuration was designed and analysed. The mechanism was modelled in three dimensions, and closed-form inverse kinematics, sphere-intersection forward kinematics and a Jacobian-based torque model were developed and checked against an independent implementation of the same equations. The reachable workspace, the static holding capacity of the specified actuator and the torque demand of five prescribed end-effector paths were evaluated. Ten candidate materials, covering wrought aluminium alloys, printing polymers, a fibre-reinforced polymer and additive-manufacturing materials, were compared through finite element static, modal and steady-state thermal analyses under identical boundary conditions. The high-strength wrought aluminium alloy gave the lowest deformation, the highest fundamental frequency and an adequate safety margin, whereas two of the polymers could not carry the design load. Topology optimization reduced the structural mass but moved the critical stress to the upper arm beyond the allowable limit, which shows that the optimized geometry must be reinforced and re-analysed before fabrication. A high-strength wrought aluminium alloy is recommended for a conventionally machined robot and an additively manufactured aluminium alloy for an optimized design.**

***Index Terms*—Delta robot, parallel manipulator, kinematics, finite element analysis, modal analysis, thermal analysis, topology optimization, material selection**

I. INTRODUCTION

Delta robots dominate high-speed pick-and-place because their three actuators are fixed to the frame and drive a light platform through parallel chains [1]. Their performance is limited less by actuator power than by the stiffness, mass and vibration of the moving links. Versions built from printed polymers or aluminium alloys make the robot accessible to laboratories and small industries, but material substitution changes deflection, strength, natural frequency and heat transfer at the same time. This paper evaluates one published geometry [2] across these effects using a single model carried from CAD through kinematics, finite element analysis and topology optimization.

The parallel layout gives the Delta robot high speed and acceleration, high stiffness, good repeatability and a simple modular construction, because the three identical branches share the load and only light links move [1, 3]. Its limitations are a small workspace relative to its size, coupled kinematics, singular configurations, a light payload with translation only, and positioning errors caused by clearance in the passive spherical joints [4, 5]. Delta robots are therefore used for pick-and-place, sorting and packaging on conveyor lines [2], for food, pharmaceutical and electronics handling, for laser cutting [6], as Delta-type 3D printers [7] and as platforms for teaching and research [8, 9].

II. LITERATURE REVIEW

Clavel's original concept established the parallelogram forearm that keeps the platform parallel to the base [1]. Workspace-driven dimensioning and dimensional synthesis were developed by Liu et al. and Laribi et al. [4, 10], and closed-form kinematic solutions are given in standard texts [3, 11]. 3D-printed Delta robots have been demonstrated for vision-guided handling, education and industrial use [2, 12, 13], although printed links are compliant [14]. Studies on serial arms show that material choice affects stress, vibration and cost together [15, 16], and that topology optimization must be followed by re-analysis because removing material redistributes stress [17–20]. Few studies combine kinematics, multi-material static, modal and thermal analysis and topology optimization for one Delta configuration under identical conditions.

III. OBJECTIVES

The published geometry demonstrated pick-and-place operation [2], but its structural, dynamic and thermal behaviour and its sensitivity to material choice were not established. The objectives were to (i) model the mechanism and verify its kinematics and workspace, (ii) estimate actuator torque, (iii) compare ten materials by static, modal and steady-state thermal finite element analysis, (iv) reduce mass by topology optimization and re-check the result, and (v) validate the numerical results against independent calculations.

IV. METHODOLOGY

The workflow is shown in Fig. 1. The CATIA assembly was exported as STEP to ANSYS Workbench and meshed with SOLID187 quadratic tetrahedra of 4 mm nominal size, giving 63,059 elements and 116,148 nodes. The base plate was fixed. The static case applied 200 N in Z at the platform handling rod together with gravity. The modal case had no external load, and the thermal case imposed 50 °C on the top of the base plate with convection (h = 5 W/m²K, T∞ = 30 °C) elsewhere. In parallel, MATLAB was used for the kinematic model, workspace and five trajectories. A failed strength, frequency or validation check returned the design to the CAD or material stage.

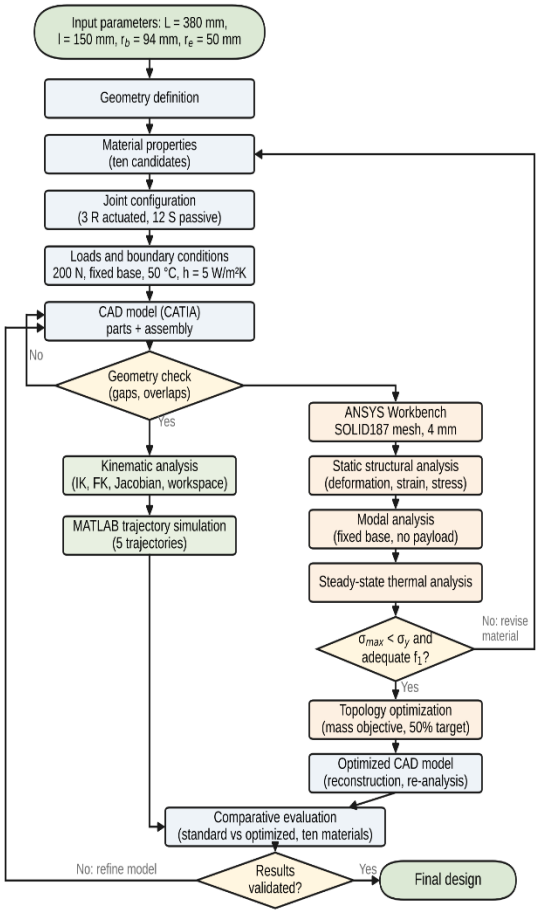

Fig. 1. Design and analysis workflow with decision points.

V. DESIGN

The robot has three identical R–(S–S) ₂ branches spaced at 120° (Fig. 2). Each actuated revolute joint on the base drives an upper arm, and a pair of forearm rods connects the elbow to the moving platform through spherical joints. The design parameters are listed in Table 1.

The mobility of the spatial mechanism follows from the Grübler–Kutzbach criterion

$$M = 6\,(N - 1 - j) + \sum_{i=1}^{j} f_i \qquad (1)$$

where N = 11 links and j = 15 joints (three revolute joints with f = 1 and twelve spherical joints with f = 3), which gives M = 6(11 − 1 − 15) + 39 = 9. Six of these freedoms are idle spins of the forearm rods about their own axes, so the effective mobility is 9 − 6 = 3,

all translational. The equivalent offset used in the kinematic equations is a = rb − re = 94 − 50 = 44 mm.

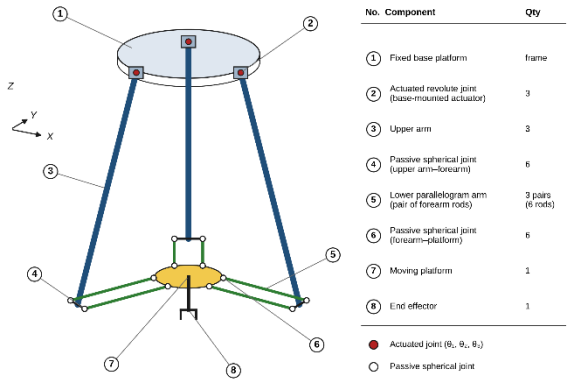

Fig. 2. Architecture of the proposed Delta robot with numbered components.

Table 1, Design parameters

Parameter	Value
Upper arm L / forearm l	380 mm / 150 mm
Base radius rb / platform radius re	94 mm / 50 mm (a = 44 mm)
Branch azimuths	0°, 120°, 240°
Actuator range	−40° to +80°
Arm section	Tube, Ø20 mm, 6 mm wall
Design load	200 N in Z

VI. KINEMATICS

In the frame of branch i, rotated by φi, the loop-closure condition reduces to a single-harmonic equation in the actuator angle:

$$E_i\cos\theta_i + F_i\sin\theta_i = G_i \quad (2)$$

which has the closed-form solution

$$\theta_i = \operatorname{atan2}(F_i, E_i) \pm \cos^{-1}\frac{G_i}{\sqrt{E_i^2+F_i^2}} \quad (3)$$

Here Ei = 2L (y'i + a), Fi = 2Lz and Gi = −(x'2i + y'2i + z2 + a2 + L2 + 2ay'i − l2). The root inside the actuator range is kept [11, 21]. The forward solution intersects three spheres of radius l centred at the elbows. Differentiating the sphere constraints gives A vP = B ω, so vP = J−1ω with J−1 = A−1B. The actuator torque follows from virtual work:

$$\tau_i = I_1\alpha_i + m_1 g\frac{L}{2}\cos\theta_i + \tau_{P,i} \quad (4)$$

where the platform term is

$$\tau_P = (J^{-1})^T M_{eff}\,(a_P + g) \quad (5)$$

Here m1 = 0.3355 kg, I1 = 0.01615 kg·m² and Meff = 0.713 kg. At P = (30, −20, −350) mm, with ω = 0.2 rad/s and α = 1 rad/s², the model gives θ = 71.1697°, 71.9046° and 79.6773°, vP = (−41.75, 28.52, 764.01) mm/s and τ = (−5.945, −5.851, −3.917) N·m. The platform term is the largest, and the upper-arm term is only 0.13–0.22 N·m. The workspace extends from z = −272 to −477 mm with a maximum reach of about 44 mm in the X–Z plane (Fig. 3), which is compact because the forearm is short.

For the forward problem, the elbow of branch i is located at

$$C_i = [\rho_i\sin\varphi_i,\ -\rho_i\cos\varphi_i,\ -L\sin\theta_i]^T \quad (6)$$

with ρi = a + L cos θi, and the platform centre P is the intersection of the three spheres

$$\|P - C_i\|^2 = l^2, \qquad i = 1,2,3 \quad (7)$$

of which the root below the base (z < 0) is retained. Differentiating these constraints gives the velocity relation

$$A\dot{P} = B\dot{\theta}, \qquad \dot{P} = J^{-1}\dot{\theta}, \qquad J^{-1} = A^{-1}B \quad (8)$$

where the rows of A are (P − Ci) T and B is diagonal. A singular A or B marks a singular configuration, which was checked along the paths through the reciprocal condition number.

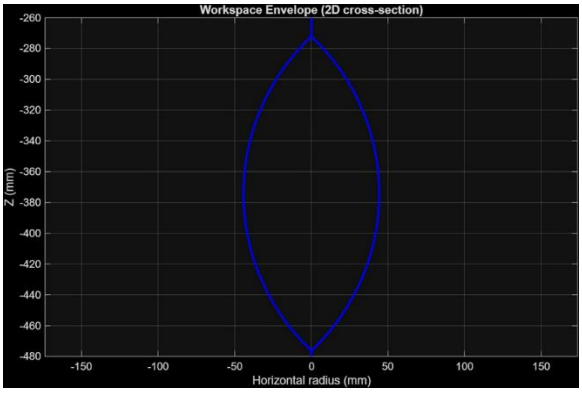

Fig. 3. Workspace envelope in the X–Z plane.

VII. PAYLOAD CAPACITY

The static payload that the specified NEMA 23 stepper motor (rated holding torque 2.2 N·m) can hold was estimated with a safety factor of 1.5. In Model A one upper arm carries the whole payload weight, and in Model B the weight is shared equally by the three arms. From the moment balance about the actuator axis [22],

$$m_A = \frac{\tau_{rated}}{g\,L\cos\theta}, \qquad m_B = \frac{3\,\tau_{rated}}{g\,L\cos\theta} \quad (9)$$

The moment of the payload weight is largest at θ = 0°, which lies inside the −40° to +80° actuator range, so this is the worst case (Table 2). The safe even-split payload there is 1.18 kg, below the 2 kg reference mass, so a stronger motor or a gear reduction is needed for a 2 kg payload.

Table 2
Static payload capacity of the NEMA 23 motor (L = 0.38 m)

Model	Angle	No SF (kg)	SF 1.5 (kg)
A: one arm	θ = 40°	0.770	0.514
B: shared by three arms	θ = 40°	2.311	1.541
A: one arm	θ = 0°	0.590	0.393
B: shared by three arms	θ = 0°	1.770	1.180

VIII. TRAJECTORY ANALYSIS

Five end-effector paths were simulated in MATLAB over 12 s each (Table 3). Velocity and acceleration were obtained by central differences, and the actuator demand was estimated by lumping a mass m = 2 kg at the tip of the upper arm and applying Newton's second law [22]:

Table 3
End-effector paths (mm, t in s)

Path	Definition	Steps
Rectangular	x = 30 square(t), y = 30 square (t + π/2), z = −450	400
Circular	x = 30 cos t, y = 30 sin t, z = −450	400
Cylindrical	r = 30, 12 turns, z = −550 to −450	800
Spherical	R = 80 about (0, 0, −450), 20 turns	800
Elliptical	x = 32 cos t, y = 20 sin t, z = −450	400

$$\tau = m\,(a + g)\,L, \qquad P_t = m\,(a + g)\,v \tag{10}$$

The peak values are listed in Table 4 and compared in Fig. 4. The circular path checks the numerical differentiation: v = rω = 30 mm/s and a = v²/r = 30 mm/s², exactly as computed. The smooth paths need about 7.5 N·m, which is almost entirely the gravity term mgL = 7.46 N·m. The square path jumps from corner to corner, so its derivatives give the largest spikes and the largest torque, 20.06 N·m; a real rectangular move would need blended corners.

Table 4
Peak values of the trajectory simulation (m = 2 kg)

Path	v (mm/s)	a (mm/s²)	τ (N·m)	F·v (W)
Rectangular	997.5	16,583.4	20.06	52.65
Circular	30.0	30.0	7.48	0.59
Cylindrical	188.6	1,180.8	8.35	4.14
Spherical	834.6	8,706.1	14.07	30.91
Elliptical	32.0	32.0	7.48	0.63

The path points were also checked against the inverse-kinematic reachability condition and the actuator range (Fig. 5). At z = −450 mm the radius reachable in every direction is only about 19.5 mm, so only 34 of 400 circle points, 139 of 400 ellipse points and 156 of 800 sphere points are reachable, and none of the square corners or helix points. The torque estimates remain valid because they depend only on path shape and timing, but the paths should be re-centred near z = −375 mm, where a 30 mm circle fits.

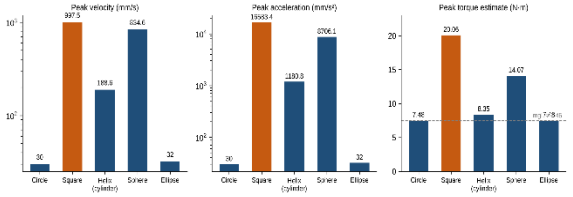

Fig. 4. Peak speed, acceleration (logarithmic scales) and torque estimate of the five trajectories.

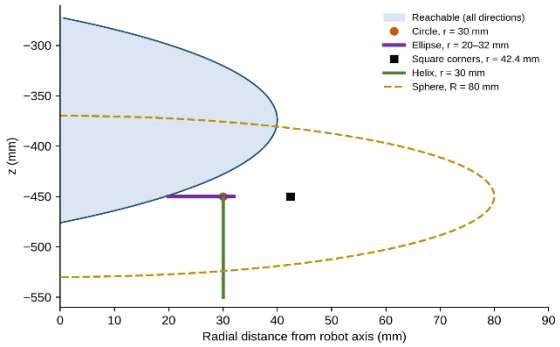

Fig. 5. Radial extent of the prescribed paths compared with the radius reachable in all directions at each height.

IX. MATERIAL SELECTION

Ten materials were selected from four groups: wrought aluminium alloys (AA 1100, AA 2011, AA 2024, AA 7075-T6), printing polymers (ABS, PETG,

PLA), a fibre-reinforced polymer (CFR nylon) and additive-manufacturing materials (AlSi10Mg, Nylon PA12). Their assigned properties are listed in Table 5. The aluminium alloys are 20 to 60 times stiffer than the polymers but only about twice as dense, so their specific stiffness is an order of magnitude higher.

Table 5
Material properties assigned in the finite element model

Material	ρ (kg/m³)	E (GPa)	ν	σy (MPa)
AA 1100	2,710	69	0.33	250
AA 2011	2,820	71	0.33	250
AA 2024	2,780	73.1	0.33	324
AA 7075-T6	2,810	71.7	0.33	250
AlSi10Mg	2,670	70	0.33	230
ABS	1,040	2.1	0.35	40
PETG	1,270	2.2	0.38	50
PLA	1,240	3.5	0.36	60
Nylon PA12	1,010	1.7	0.39	48
CFR nylon	1,350	1.2	0.30	110

X. FINITE ELEMENT MODEL

The finite element method divides the structure into elements connected at nodes and solves the discretised equations for the nodal unknowns [23]. The imported assembly, the SOLID187 mesh and the boundary conditions are shown in Fig. 6, and the conditions of each analysis are summarised in Table 6. The same geometry and mesh were used for every material, so differences in response come from the material properties alone.



Fig. 6. Finite element set-up: (a) imported geometry, (b) tetrahedral mesh and (c) boundary conditions and loading.

Table 6
Boundary conditions of the finite element analyses

Analysis	Support	Loads / conditions	Outputs
Static	Fixed base	200 N in Z at handling rod; gravity	Deformation, strain, von Mises stress
Modal	Fixed base	No external load	Frequencies and mode shapes
Thermal	–	50 °C at base top; h = 5 W/m²K, T∞ = 30 °C	Temperature, heat flux
Topology	Fixed base; joints excluded	200 N; 50 % mass target	Optimized layout

Strength is judged with the von Mises equivalent stress, and the factor of safety against yielding is the ratio of the yield strength to the maximum equivalent stress [24]:

$$\sigma_{eq} = \sqrt{\frac{(\sigma_1-\sigma_2)^2+(\sigma_2-\sigma_3)^2+(\sigma_3-\sigma_1)^2}{2}} \quad (11)$$

$$FS = \frac{\sigma_y}{\sigma_{max}} \quad (12)$$

XI. STRUCTURAL ANALYSIS

The linear static problem [K]{u} = {F} was solved for each material, and the factor of safety was obtained as FS = σy/σmax. The AA 7075-T6 contours are shown in Fig. 7 and all results are listed in Table 7. The maximum stress is almost independent of material (49.5–50.4 MPa) because the supports and load are fixed [23], so each material is judged by its own yield strength [24]. Deformation, however, scales inversely with stiffness (Fig. 8).

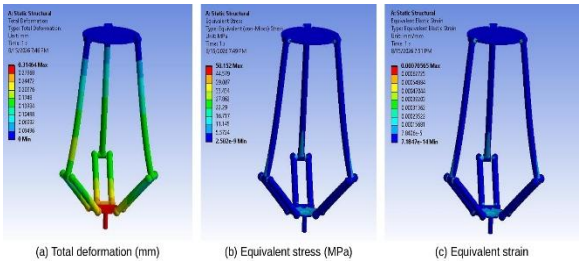

Fig. 7. AA 7075-T6 assembly under 200 N: (a) total deformation, (b) equivalent stress, (c) equivalent strain.

Table 7
Static results for the complete assembly under 200 N

Material	δmax (mm)	σmax (MPa)	FS
AA 1100	0.327	50.15	4.98
AA 2011	0.318	50.15	4.98
AA 2024	3.09	50.15	6.46
AA 7075-T6	0.315	50.15	4.98
AlSi10Mg	3.22	50.15	4.59
ABS	10.73	49.96	0.80
PETG	10.21	49.60	1.01
PLA	6.43	49.85	1.20
Nylon PA12	13.19	49.46	0.97
CFR nylon	18.81	50.39	2.18

Deformation exported from ANSYS in metres and converted to mm. The AA 2024 and AlSi10Mg values are provisional: the ANSYS material data show Young's modulus entered as 7.31 × 109 Pa (AA 2024) and 7.0 × 109 Pa (AlSi10Mg), ten times too low.

The AA 2024 and AlSi10Mg deformations (3.09 and 3.22 mm) are about ten times those of the other aluminium alloys. The ANSYS material data show why: Young's modulus was entered as 7.31 × 109 Pa for AA 2024 and 7.0 × 109 Pa for AlSi10Mg instead of about 73.1 GPa and 70 GPa. Their stresses are unaffected, because the stress depends mainly on load and geometry, but their deformation and frequency results are provisional and must be re-run.

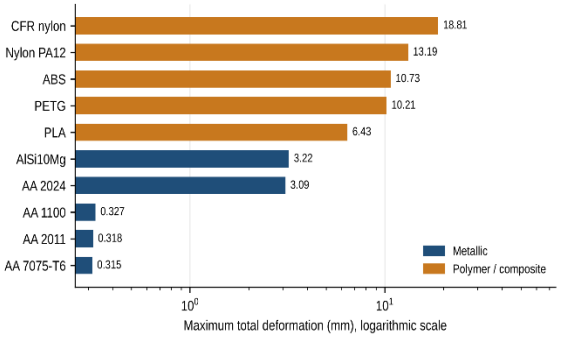

Fig. 8. Assembly deformation by material (logarithmic scale).

XII. MODAL ANALYSIS

The undamped eigenproblem ([K] − ωn2[M]) {φn} = 0 was solved with a fixed base and no payload. The first three frequencies are given in Table 8. AA 7075-T6 has the highest fundamental frequency, 45.77 Hz, with a close second mode at 46.39 Hz, as expected from the three-fold symmetry. The polymer fundamentals scale with √(E/ρ) [25]. For PLA, for example, both the predicted and the computed ratio to AA 7075-T6 are 0.33. The AA 2024 and AlSi10Mg values (about 14.7 Hz) are low by about √10 because of the modulus input error. All values are numerical and would need a modal test to confirm, since joints and real supports shift measured frequencies [26].

Table 8
First three natural frequencies of the assembly (Hz)

Material	f1	f2	f3
AA 1100	45.72	46.34	115.02
AA 2011	45.46	46.08	114.38
AA 2024	14.69	14.89	36.97
AA 7075-T6	45.77	46.39	115.15
AlSi10Mg	14.67	14.87	36.91
ABS	12.89	13.06	32.39
PETG	11.97	12.13	30.03
PLA	15.25	15.46	38.30
Nylon PA12	11.81	11.98	29.63
CFR nylon	8.54	8.65	21.52

The first five distinct mode shapes of the AA 7075-T6 assembly are shown in Fig. 9. The low modes are lateral swings of the platform on the three branches, while the higher modes involve bending of the upper arms and forearm rods.

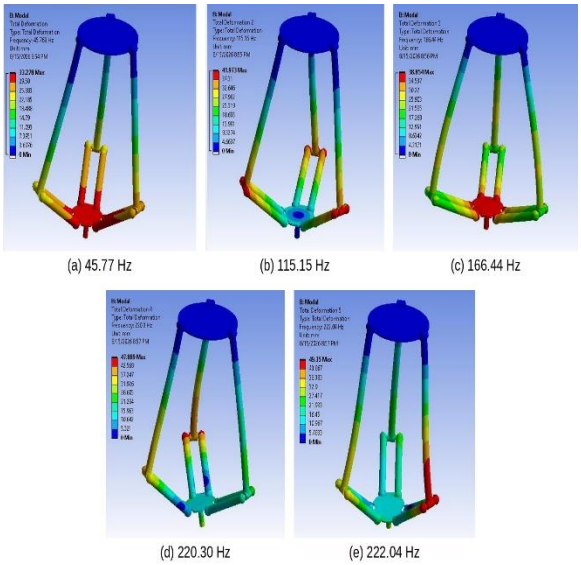

Fig. 9. Mode shapes of the AA 7075-T6 assembly at (a) 45.77 Hz, (b) 115.15 Hz, (c) 166.44 Hz, (d) 220.30 Hz and (e) 222.04 Hz.

XIII. THERMAL ANALYSIS

Heat transfer in the solid follows Fourier's law, and the exposed surfaces exchange heat with the air by convection [27]:

$$q'' = -k\nabla T, \qquad q'' = h\,(T_s - T_\infty) \qquad (13)$$

Motor heating was represented by 50 °C on the top of the base plate, with convection elsewhere. The aluminium alloys carried 39.7–52.9 kW/m² and warmed the lowest point of the robot to 32.6–35.0 °C. The polymers carried 0.79–2.05 kW/m² and remained at the 30 °C ambient away from the base (Fig. 10). AA 1100 spreads the heat best, in line with its higher conductivity [27]. These are comparative results under prescribed boundary conditions, not predictions of motor temperature.

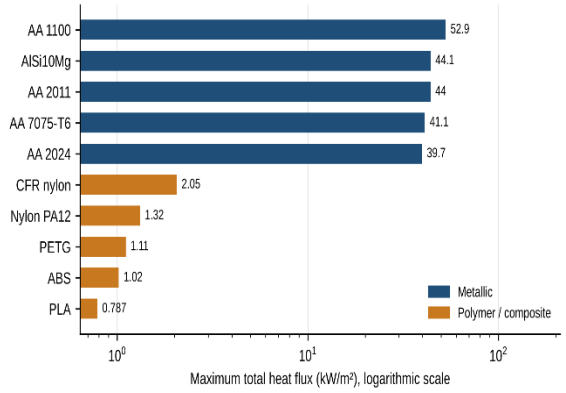

Fig. 10. Maximum heat flux through the assembly by material.

The temperature and heat-flux distributions of AA 7075-T6 are shown in Fig. 11, and the results of all materials are listed in Table 9.

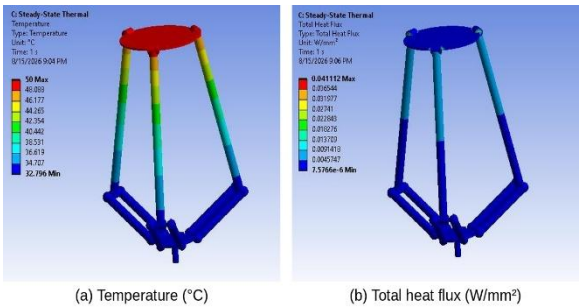

Fig. 11. Steady-state thermal results for the AA 7075-T6 assembly: (a) temperature and (b) total heat flux.

Table 9
Steady-state thermal results (50 °C at base, h = 5 W/m²K)

Material	qmax (kW/m²)	Tmax (°C)	Tmin (°C)
AA 1100	52.92	50.0	35.01
AA 2011	44.04	50.0	33.32
AA 2024	39.72	50.0	32.55
AA 7075-T6	41.11	50.0	32.80
AlSi10Mg	44.07	50.0	33.32
ABS	1.020	50.0	30.00
PETG	1.108	50.0	30.00
PLA	0.787	50.0	30.00
Nylon PA12	1.319	50.0	30.00
CFR nylon	2.053	50.0	30.00

XIV. TOPOLOGY OPTIMIZATION

In the density-based approach each element of the design region carries a pseudo-density ρe between a small lower bound and 1, and its stiffness is interpolated with a penalty exponent p > 1 so that intermediate densities are driven towards solid or void [28]:

$$E(\rho_e) = \rho_e^{p}\, E_0, \qquad 0 < \rho_{min} \le \rho_e \le 1 \qquad (14)$$

The mass reduction, with ms the standard mass and mo the optimized mass, is evaluated as

$$\Delta m = \frac{m_s - m_o}{m_s} \times 100 \qquad (15)$$

The standard and optimized assemblies are compared in Fig. 12, and the modal total-deformation contours of the AA 7075-T6 components before and after optimization are shown in Fig. 13. The optimized arms and plates show the porous shape left by the density-based removal, while the joint seats keep their original form.

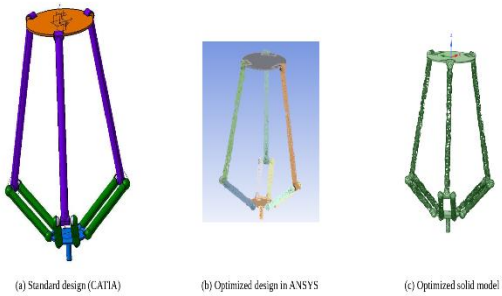

Fig. 12. Assembly models: (a) standard design, (b) topology-optimized design and (c) optimized solid model after STL-to-solid conversion.

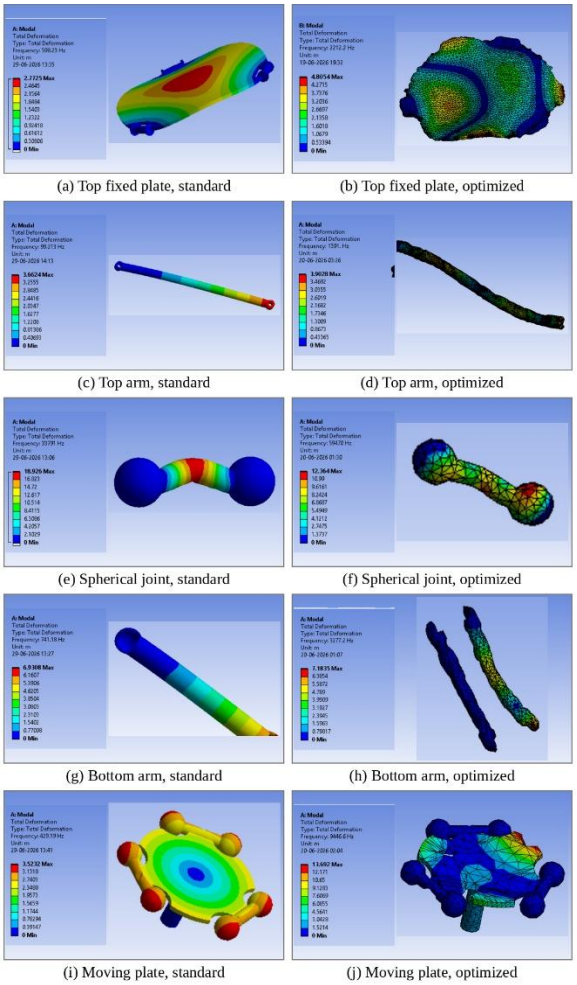

Fig. 13. Modal total-deformation contours of the AA 7075-T6 components, standard (left) and topology-optimized (right) designs.

Density-based topology optimization [28] was run with mass and stress as design functions and a 50 % mass-reduction target, with the supports and joints excluded from the design region. After reconstruction, the tube wall was 4 mm instead of 6 mm, and the mass fell from 2.1458 kg to 1.9308 kg, a reduction of 10.02 %. The joint and manufacturability constraints account for the gap to the target. The component-level comparison for AA 7075-T6 (Fig. 14, Table 10) shows that the critical member moves from the bottom arm (130.0 MPa) to the top arm (318.4 MPa). This exceeds the assigned yield strength of AA 7075-T6 (FS = 0.79), so, as in other robot lightweighting studies [18, 19], the optimized part must be re-checked and reinforced.

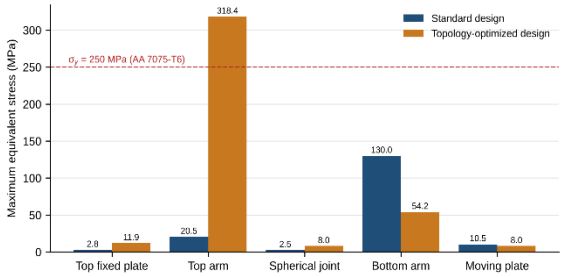

Fig. 14. Component stress before and after optimization (AA 7075-T6).

Table 10
AA 7075-T6 components: standard (S) and optimized (O) designs

Component	δS (mm)	δO (mm)	σS (MPa)	σO (MPa)	f1, S (Hz)	f1, O (Hz)
Top fixed plate	0.0009	0.0038	2.84	11.89	598.2	701.7
Top arm	1.458	5.543	20.51	318.37	99.2	73.3
Spherical joint	0.0011	0.0036	2.50	7.99	33,790	24,100
Bottom arm	0.444	0.706	129.99	54.16	741.2	477.8
Moving plate	0.030	0.014	10.49	7.99	429.2	3,064

XV. RESULTS AND DISCUSSION

AA 7075-T6, AA 2011 and AA 1100 form a group of stiff, adequately strong and inexpensive materials. AA 7075-T6 is preferred because it combines the lowest deformation, the highest fundamental frequency and an FS of about 5 (Table 11). Among the polymers only PLA (FS 1.20) and CFR nylon (FS 2.18) keep a margin, and their deformations of 6.4–18.8 mm and fundamentals below 16 Hz rule them out except for light-duty prototypes. The optimized design reduces inertia, but it is not yet acceptable structurally. AlSi10Mg, suited to producing organic optimized shapes by laser powder-bed fusion [20], is the natural additive route once the top arm is reinforced and its stiffness results are re-run with the correct modulus.

Here cost refers to material and fabrication cost, not the full system price.

Table 11
Summary of results for material selection

Material	δ (mm)	FS	f1 (Hz)	q (kW/m²)	Cost
AA 7075-T6	0.315	4.98	45.77	41.11	Low
AA 1100	0.327	4.98	45.72	52.92	Low
AA 2011	0.318	4.98	45.46	44.04	Low–med
AA 2024	3.09*	6.46	14.69*	39.72	Low
AlSi10Mg	3.22*	4.59	14.67*	44.07	High
PLA	6.43	1.20	15.25	0.787	Low–med
CFR nylon	18.81	2.18	8.54	2.053	High
PETG/ABS/PA12	10.2–13.2	0.80–1.01	11.8–12.9	1.0–1.3	Low–high

Provisional (modulus input error)

XVI. VALIDATION

The MATLAB model was checked against an independent implementation of the same equations (Table 12), with difference = |theoretical − MATLAB|/|theoretical| × 100. The forward kinematics closed the inverse solution to 5.6 × 10−13 mm. Hand checks on a solid Ø20 mm upper arm loaded by τplat/L = 16.2 N gave a root stress of 7.85 MPa and a tip deflection of 0.527 mm (k = 30.79 N/mm). The forearm Euler load was 241 kN, so buckling is not critical. The hand stress is lower than the 50 MPa finite element maximum because the beam model omits joint stress concentrations and the full 200 N load. It is therefore used as an order-of-magnitude check, not as a percentage comparison. No physical prototype was tested, so accuracy and repeatability remain to be measured.

Table 12
Independent (theoretical) versus MATLAB results

Quantity	Theoretical	MATLAB	Diff. (%)
θ1, θ2, θ3 (°)	71.1697, 71.9046, 79.6773	71.1697, 71.9046, 79.6773	0.00
τ1 (N·m)	−5.928	−5.945	0.29
τ2 (N·m)	−5.832	−5.851	0.33
τ3 (N·m)	−3.910	−3.917	0.18
Workspace height (mm)	203	205	0.99
Reach in X–Z plane (mm)	44.3	44	0.68

XVII. LIMITATIONS AND SCOPE

The 200 N load is a design case and not a measured payload rating, and the thermal model uses a prescribed base temperature rather than actual motor losses. The AA 2024 and AlSi10Mg stiffness results are provisional, the prescribed trajectories lie largely outside the workspace, and the acceleration model neglects the velocity-product term. No prototype was tested. Future work should build the AA 7075-T6 robot and measure its accuracy, repeatability, deflection, natural frequencies and temperatures, re-run the two alloys with the correct modulus, reinforce and re-optimize the top arm with a stress limit, re-centre the trajectories near z = −375 mm, size the motor or gearing for a 2 kg payload, and develop closed-loop control with trajectory smoothing.

XVIII. CONCLUSION

1) The adopted geometry provides three translational freedoms and a compact workspace about 205 mm deep with a 44 mm reach. The kinematic model was reproduced independently within 0.33 %.
2) Under 200 N, AA 7075-T6 deforms 0.315 mm with FS = 4.98 and has f1 = 45.77 Hz. ABS and Nylon PA12 have FS below 1.

3) The aluminium alloys carry about 20 to 70 times the heat flux of the polymers under the same base temperature.
4) Topology optimization saved 10.02 % of the mass but overstressed the top arm (318.4 MPa), so the optimized design needs reinforcement.
5) The specified motor supports about 1.18 kg at the worst arm angle, and the prescribed trajectories need re-centring inside the workspace.
6) AA 7075-T6 is recommended for machining and AlSi10Mg for additive manufacturing. Prototype testing of accuracy, repeatability, vibration and temperature is the next step.

REFERENCES

[1] R. Clavel, "DELTA, a fast robot with parallel geometry," in Proc. 18th International Symposium on Industrial Robots, Lausanne, Switzerland, Apr. 1988, pp. 91–100.

[2] L. H. Phuong, V. D. Cong, and T. T. Hiep, "Design a low-cost delta robot arm for pick and place applications based on computer vision," FME Transactions, vol. 51, no. 1, pp. 99–108, 2023, doi: 10.5937/fme2301099P.

[3] J.-P. Merlet, Parallel Robots, 2nd ed. Dordrecht, The Netherlands: Springer, 2006.

[4] X.-J. Liu et al., "A new approach to the design of a DELTA robot with a desired workspace," Journal of Intelligent and Robotic Systems, vol. 39, no. 2, pp. 209–225, 2004, doi: 10.1023/B:JINT.0000015403.67717.68.

[5] Gao and Wang, "Design, manufacturing, and visual servoing of a 3D-printed delta robot," in Proc. IEEE Canadian Conference on Electrical and Computer Engineering (CCECE), 2024, pp. 769–773, doi: 10.1109/CCECE59415.2024.10667084.

[6] Moharana et al., "Optimization and design of a laser-cutting machine using delta robot," International Journal of Engineering Trends and Technology, vol. 10, no. 4, pp. 176–179, doi: 10.14445/22315381/IJETT-V10P233.

[7] Hsieh et al., "Investigation of delta robot 3D printer for a good quality of printing," Applied Mechanics and Materials, vol. 870, pp. 164–169, 2017, doi: 10.4028/www.scientific.net/AMM.870.164.

[8] Chavdarov et al., "3D printed DELTA robot for educational purposes," 2024. Publication venue not specified.

[9] Lin et al., "Design and implementation of a new DELTA parallel robot in robotics competitions," International Journal of Advanced Robotic Systems, 2015, doi: 10.5772/61744.

[10] M. A. Laribi, L. Romdhane, and S. Zeghloul, "Analysis and dimensional synthesis of the DELTA robot for a prescribed workspace," Mechanism and Machine Theory, vol. 42, no. 7, pp. 859–870, 2007, doi: 10.1016/j.mechmachtheory.2006.06.012.

[11] R. L. Williams II, "The Delta parallel robot: Kinematics solutions," Ohio University, Athens, OH, USA, online publication, Oct. 2016.

[12] C. M. A. Vasques and F. A. V. Figueiredo, "The 3D-printed low-cost delta robot Óscar: Technology overview and benchmarking," in Proc. 2nd International Electronic Conference on Applied Sciences, Engineering Proceedings, vol. 11, no. 1, Art. no. 43, 2021, doi: 10.3390/ASEC2021-11173.

[13] Islam et al., "Design and development of a low-cost 3-DOF delta robot for industrial application: A comprehensive analysis," Journal of Engineering Research and Reports, vol. 27, no. 5, pp. 285–296, 2025, doi: 10.9734/jerr/2025/v27i51507.

[14] P. Mannam, O. Kroemer, and F. Z. Temel, "Characterization of compliant parallelogram links for 3D-printed delta manipulators," in Experimental Robotics: Proceedings of the 17th International Symposium on Experimental Robotics (ISER 2020), Springer Proceedings in Advanced Robotics. Cham, Switzerland: Springer, 2021.

[15] Yin et al., "Hybrid structure design of lightweight robotic arms based on carbon fiber reinforced plastic and aluminum alloy," IEEE Access, vol. 7, pp. 64932–64945, 2019, doi: 10.1109/ACCESS.2019.2915363.

[16] S. A. Kouritem et al., "A multi-objective optimization design of industrial robot arms," Alexandria Engineering Journal, vol. 61, no. 12, pp. 12847–12867, 2022, doi: 10.1016/j.aej.2022.06.052.

[17] Wang et al., "Optimal design of lightweight serial robots by integrating topology optimization

and parametric system optimization," Mechanism and Machine Theory, vol. 132, pp. 48–65, 2019, doi: 10.1016/j.mechmachtheory.2018.10.015.

[18] Sha et al., "A topology optimization method of robot lightweight design based on the finite element model of assembly and its applications," Science Progress, vol. 103, no. 3, 2020, doi: 10.1177/0036850420936482.

[19] M. Alshihabi, M. Özkahraman, and M. Kayacan, "Enhancing the reliability of a robotic arm through lightweighting and vibration control with modal analysis and topology optimization," Mechanics Based Design of Structures and Machines, vol. 53, no. 3, pp. 1950–1974, 2025, doi: 10.1080/15397734.2024.2400207.

[20] R. C. Batista et al., "Topological and lattice-based AM optimization for improving the structural efficiency of robotic arms," Frontiers in Mechanical Engineering, vol. 10, Art. no. 1422539, 2024, doi: 10.3389/fmech.2024.1422539.

[21] L.-W. Tsai, Robot Analysis: The Mechanics of Serial and Parallel Manipulators. New York, NY, USA: Wiley, 1999.

[22] J. J. Craig, Introduction to Robotics: Mechanics and Control, 4th ed. New York, NY, USA: Pearson, 2018.

[23] R. D. Cook, D. S. Malkus, M. E. Plesha, and R. J. Witt, Concepts and Applications of Finite Element Analysis, 4th ed. New York, NY, USA: Wiley, 2002.

[24] R. G. Budynas and J. K. Nisbett, Shigley's Mechanical Engineering Design, 11th ed. New York, NY, USA: McGraw-Hill, 2020.

[25] S. S. Rao, Mechanical Vibrations, 6th ed. Hoboken, NJ, USA: Pearson, 2017.

[26] Martínez-Cruz et al., "Natural frequencies identification by FEM applied to a 2-DOF planar robot and its validation using MUSIC algorithm," Sensors, vol. 21, no. 4, Art. no. 1209, 2021, doi: 10.3390/s21041209.

[27] T. L. Bergman, A. S. Lavine, F. P. Incropera, and D. P. DeWitt, Fundamentals of Heat and Mass Transfer, 7th ed. Hoboken, NJ, USA: Wiley, 2011.

[28] M. P. Bendsøe and O. Sigmund, Topology Optimization: Theory, Methods, and Applications. Berlin, Germany: Springer, 2003.